Molecular origins of anisotropic shock propagation in crystalline and amorphous polyethylene

Thomas C. O'Connor,[1,*] Robert M. Elder,[2,3,†] Yelena R. Sliozberg,[2,4] Timothy W. Sirk,[2]
Jan W. Andzelm,[2] and Mark O. Robbins[1,‡]

[1]*Department of Physics and Astronomy, Johns Hopkins University, Baltimore, Maryland 21218, USA*
[2]*U.S. Army Research Laboratory, Aberdeen Proving Ground, Maryland 21005, USA*
[3]*Bennett Aerospace, Inc., Cary, North Carolina 27511, USA*
[4]*SURVICE Engineering Company, Belcamp, Maryland 21017, USA*

Molecular dynamics simulations are used to analyze shock propagation in amorphous and crystalline polyethylene. Results for the shock velocity U_s are compared to predictions from Pastine's equation of state and hydrostatic theory. The results agree with Pastine at high impact velocities. At low velocities the yield stress becomes important, increasing the shock velocity and leading to anisotropy in the crystalline response. Detailed analysis of changes in atomic order reveals the origin of the anisotropic response. For shock along the polymer backbone, an elastic front is followed by a plastic front where chains buckle with a characteristic wavelength. Shock perpendicular to the chain backbone can produce plastic deformation or transitions to different orthorhombic or monoclinic structures, depending on the impact speed and direction. Tensile loading does not produce stable shocks: Amorphous systems craze and fracture while for crystals the front broadens linearly with time.

I. INTRODUCTION

In the last forty years, we have seen great advances in our ability to draw and align long linear polymers such as polyethylene (PE) into highly oriented fibers and films. These highly anisotropic materials have stiffnesses comparable to steel but are much cheaper to process and incorporate into cables, fabrics, and composites [1–5]. Drawn PE materials are found in a growing number of mechanically demanding applications—ship sails, vehicular chassis, prosthetic joints, and body armors—which often fail when mechanical shock waves are generated by sudden impacts. Improving applications requires a better understanding of how shocks propagate through aligned PE and how mechanical energy is dissipated by plastic mechanisms.

While the phenomenology of shock propagation in hydrostatic fluids and isotropic solids is well developed, these theories are not easily adapted to highly anisotropic solids such as polymer crystals, where direction-dependent mechanics and plastic yield are important. The heterogeneous structure of drawn PE makes experimental measurements of shock propagation in specific phases challenging. Micromechanical models often aid interpretation of experiments but they require accurate constitutive laws for PE's crystalline and amorphous phases [1,6]. Given the analytic challenges, few constitutive laws have been developed, and the most widely used theory for shock in crystalline and amorphous PE, derived by Pastine nearly 50 years ago, only considers hydrostatic loading (no

shear stress) [7,8]. Such hydrostatic laws neglect the shear strength of materials. They work well for high-velocity impact when shock stresses exceed the yield stress and plastically "fluidize" material, but they ignore the detailed effects of anisotropy, material strength, and plasticity [9].

Molecular dynamics (MD) simulations have proven a useful tool for studying the effect of material strength on shock [10–21], but few MD potentials accurately describe PE at the large pressures produced in shocks. The AIREBO-M reactive potential for hydrocarbons was developed to address this challenge [22]. It agrees with x-ray measurements of crystalline PE structure up to ∼40 GPa and gives an equation of state that is consistent with Pastine's hydrostatic theory for shock of crystalline PE [22].

In this paper, AIREBO-M is used in dynamic impact simulations to generate and characterize shock wave propagation in amorphous PE and crystalline PE along its 3 principal axes. The complexity of the response is illustrated by the plot of shock velocity U_s against impact velocity U_p in Fig. 1. The results for strong shocks are consistent with Pastine's hydrostatic calculations. Shocks travel faster through the crystal because of its higher density and ordered structure. As the impact velocity decreases, the yield stress becomes important, leading to deviations from Pastine's curve and strong anisotropy in the crystal response. We identify the Hugoniot elastic limit in each direction—the maximum shock pressure that produces completely recoverable deformation. We then follow molecular trajectories to characterize the direction-dependent modes of plasticity above the elastic limit and the approach to hydrostatic behavior. Shock along the chain backbone direction [001] produces an elastic front followed by a plastic shock front that buckles chains. Shock along the perpendicular axes leads to plastic deformation at low impact velocities and phase

---

*toconnor@jhu.edu
†robert.elder26.ctr@mail.mil
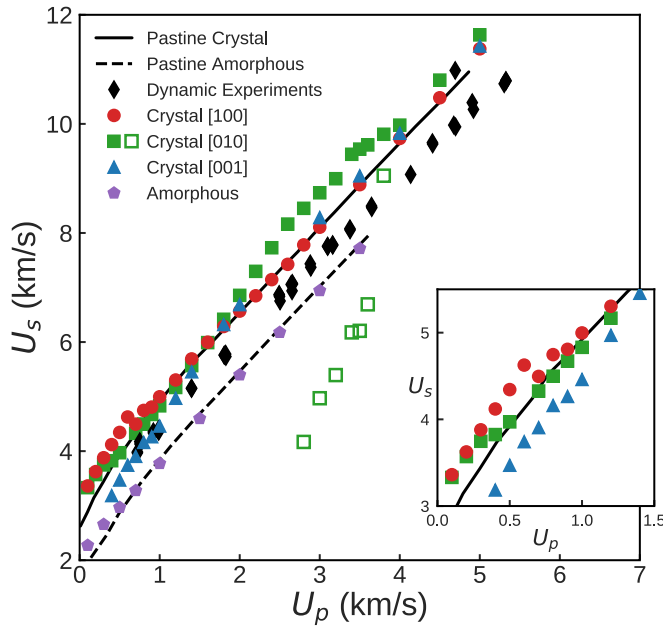‡mark.o.robbins@jhu.edu

FIG. 1. Shock velocity U_s versus impact velocity U_p in different polyethylene phases. Experimental data (black diamonds) for semicrystalline PE was used by Carter and Marsh to validate Pastine's hydrostatic models for pure crystal (black solid line) and pure amorphous (black dashed line) PE [6–8]. Colored symbols (legend) show our dynamic simulation results for amorphous PE and crystalline PE shocked along the three principle lattice directions. For strong shock, plasticity relaxes the shear stress and our simulations follow Pastine's hydrostatic models. For weak shocks (inset) simulations show deviations from hydrostatic models due to material strength. A pair of shock fronts are observed in the [010] direction at intermediate velocities. They merge into a single front when $U_p \geqslant 4.0$ km/s. A phase transition occurs at the first front (filled symbols) and plastic yield at the second (open symbols).

transitions to different crystal structures at higher U_p. For shock along the *b* axis [010], the phase transition suppresses plastic deformation, leading to separate transition and plastic shock fronts at intermediate U_p.

In the next section, we briefly review the formalism of solid shock and previous efforts to model shock in PE. Section III details our simulation and analysis methods, and Sec. IV contains detailed analysis for impacts in each phase and crystal orientation. We highlight our results and comment on their implications in Sec. V.

II. THEORY AND MODELING OF SHOCK IN PE

We consider the simple case of one-dimensional loading where a rigid body moving at impact speed U_p along the *z* direction contacts a stationary sample along a planar interface normal to the *z* direction (Fig. 2). Impact generates a planar shock front traveling into the sample at speed U_s along the *z* axis. The shock front separates regions near the impactor moving at mean particle velocity U_p from quiescent regions with mean velocity zero. In the more general case of a nonrigid impactor, deformation of the impactor leads to reduced momentum transfer and the material is accelerated to a particle velocity U_p that is lower than the initial velocity of
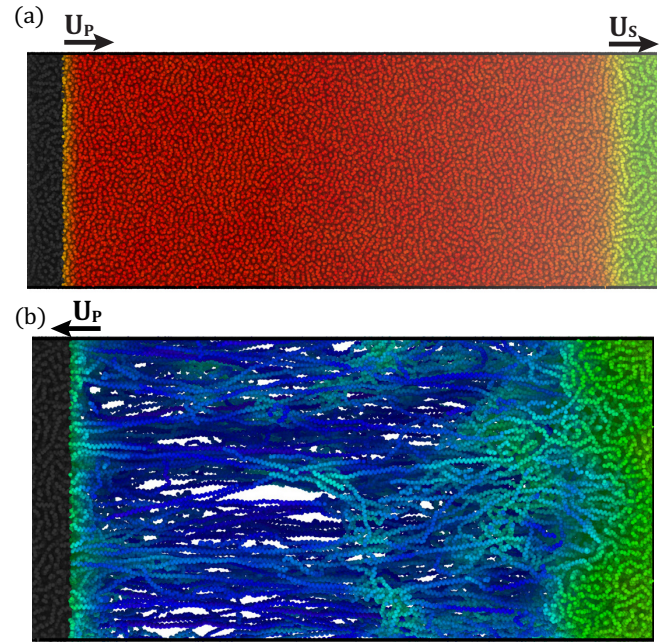

FIG. 2. Snapshots of amorphous PE configurations illustrating shock generation. After equilibration, atoms within 2.5 nm of the ends of the sample are constrained to move as rigid slabs along the horizontal *z* axis. (a) Compressive loading obtained by moving the left slab to the right at $U_p = 1.5$ km/s produces a shock propagating to the right at $U_s \approx 4.6$ km/s. (b) Tensile loading obtained by moving the left slab to the left at speed $U_p = 1.5$ km/s does not produce a stable shock. The system forms a craze and then fails. Configurations are colored qualitatively by the local density of atoms—low (blue) to high (red). Amorphous system dimensions are $16.6 \times 16.6 \times 155$ nm. Only the leftmost 47 nm and 35 nm are shown for (a) and (b), respectively.

the impactor. The specific U_p depends on the relative shock impedances of the impactor and sample [23,24].

As the shock front propagates into the sample, conservation of hydrodynamic variables, mass, momentum, and energy, imposes three "jump conditions" on the change in mass density ρ, internal energy density e, and normal stress σ_{zz} across the shock front. These Rankine-Hugoniot conditions can be written as

$$\rho_1 U_s = \rho_2 (U_s - U_p), \tag{1}$$

$$\rho_1 U_s U_p = \sigma_{2,zz} - \sigma_{1,zz}, \tag{2}$$

$$\sigma_{2,zz} U_p = U_s \left(\frac{1}{2} \rho_1 U_p^2 + e_2 - e_1 \right), \tag{3}$$

where subscripts 1 and 2 denote values in the initial and final states, respectively.

More information is needed to determine the final state and U_s for a given impact velocity. It is common to assume that the system rapidly approaches a local equilibrium state behind the shock front. Then the equation of state (EOS) of the material can be used to relate ρ, e, and the stress. Pastine's curves in Fig. 1 assume that the stress tensor is isotropic so $\sigma_{2,zz}$ equals the hydrostatic pressure P. This condition is valid for fluids,

and becomes valid for solids when σ_{zz} is much larger than the yield stress. For weaker shocks the full constitutive law must be used and the response may become anisotropic.

For shock studies of solids, the stress state is often characterized by the longitudinal shock stress amplitude $\sigma \equiv \sigma_{2,zz}$ and characteristic shear stress: $\tau \equiv \sigma_{2,zz} - \frac{1}{2}(\sigma_{2,xx} + \sigma_{2,yy})$ [20,25]. A state with shear stress $\tau = 0$ corresponds to the case of purely hydrostatic loading considered by Pastine. In the limit of linear elasticity, shocks are acoustic pulses traveling at the adiabatic sound speed c_s and τ/σ is determined by the Poisson's ratio. In anisotropic elastic solids, both c_s and τ depend on the direction of impact, producing coupling between longitudinal and transverse waves that can permit complex, mixed-mode elastic fronts [26].

Sufficiently strong impacts activate plasticity and yield in solids. The smallest shock stress that activates plastic yield, σ_{HEL}, is called the Hugoniot elastic limit (HEL)—a critical parameter for applications [23,24]. Yield causes a qualitative change in material response which can result in a two-wave elastic-plastic front structure [23,24]. The elastic front elevates σ to σ_{HEL}. The plastic front follows, mediated by activation of plastic mechanisms [23,24]. Increasing U_p increases the speed of the plastic front which may eventually overtake the elastic front [23,24]. Shocks with only a plastic front are called "overdriven" [23,24]. Multifront structures can also form when shocks drive solid-solid phase transitions. In such cases, elastic, phase transition, and plastic fronts can all propagate simultaneously [24,27].

In many cases, shock-induced plasticity above σ_{HEL} leads to a fairly constant shear stress, while σ continues to rise with U_p. As the shock strength increases, τ/σ becomes much less than unity, implying that the material flows like a fluid to reach a hydrostatic stress state as assumed by Pastine. In this regime one often finds a linear relationship between U_s and U_p. More relevant to many applications are weak shocks near the HEL where $\tau/\sigma \sim 1$. In this limit, shock propagation is nontrivially coupled to the kinematics of specific plastic mechanisms [10,11].

The combined nonlinearities of shock and plasticity make weak shocks difficult to study analytically. Materials such as crystalline PE are especially challenging, since the large mechanical anisotropy produces anisotropic plasticity as well as elastic instabilities at long length scales [28]. Consequently, analytic models have focused on the hydrostatic limit of strong shock. The most successful hydrostatic theory is the semiempirical derivation of Pastine. Pastine derived quasistatic and shock Hugoniot equations of state for crystalline and amorphous phases of PE [7,8]. Carter and Marsh later showed that mixing Pastine's models for different phases quantitatively reproduces experimental shock Hugoniot data for semicrystalline PE [6]. Semicrystalline PE is well described by hydrostatic theory since the soft amorphous phase yields isotropically for $\tau > 100$ MPa [29], leading to effective hydrostatic loading for shocks with $U_p \geqslant 0.75$ km/s.

With the expanding applications of drawn PE, there is renewed interest in extending models to weak shocks. Progress requires anisotropic characterization of the crystalline and amorphous phases, but this is very difficult to accomplish experimentally. Instead, many have turned to molecular simulation, which has proven an effective method for studying weak

shock and plasticity in many materials [10–21]. Several MD studies have investigated shock propagation in semicrystalline and amorphous PE [21,30], and amorphous composites [20] of PE using coarse-grained or united-atom potentials. Such studies give useful insight into molecular mechanisms of shock deformation, but do not provide quantitatively accurate equations of state and specific heats. For example, existing coarse-grained potentials give the wrong equilibrium crystal structure of PE and thus would not reproduce the plastic deformation mechanisms discussed below. The need for accurate atomistic potentials is well illustrated by the recent work of Mattsson *et al.* [31]. They measured the hydrostatic ($\tau = 0$) shock Hugoniot of crystalline PE with quasistatic methods that do not explicitly model dynamic impact. Comparing Hugoniots for a variety of atomistic potentials, they found most overpredict the material stiffness at pressures above 1 GPa. While some coarse-grained models may capture the material stiffness, they typically underestimate e and the specific heat because they do not include energy flow into internal vibrations, although some advanced constant-energy variants can capture these effects [32].

The need for quantitatively accurate potentials motivated the recent development of the AIREBO-M reactive potential for hydrocarbons [22]. AIREBO-M's intermolecular interactions are fitted to post-Hartree-Fock quantum calculations for the interactions of small alkane dimers. With only this training set, AIREBO-M reproduces the anisotropic deformation of crystalline PE seen in diamond anvil experiments, as well as Pastine's hydrostatic theory up to 40 GPa [22]. This means AIREBO-M accurately models the strong shock regime seen in experiments. In this paper we use AIREBO-M to explore weak shocks in purely crystalline and amorphous phases of PE.

III. METHODS

A. Atomic potential and integration

We model polyethylene with the AIREBO-M potential using the LAMMPS software package [22,33]. In the standard LAMMPS distribution, covalent interactions are modeled by the second-generation REBO (REBO2) of Brenner *et al.* [34], which is known to overpredict the tensile forces for covalent bond breaking [35]. The binding energy is correct but the interaction range is too short by 2 Å, so the C-C dissociation forces are too large. Pastewka *et al.* have created a bond-screening modified REBO2 (REBO2+S), which remedies this cutoff scheme for C-C dissociation [35]. This covalent potential was used in calibrating AIREOB-M [22] and to model tensile failure of PE [36].

We use AIREBO-M with the REBO2+S covalent terms for all tensile loading simulations because bond breaking occurs. For compressive shock, no bond breaking was observed, so we use the faster unscreened potential. We verified that for the highest impact velocity studied, 5 km/s, screened and unscreened potentials gave consistent results and that backbone C-C bonds remained in the range of separations where the two potentials are the same. The maximum temperature rises rapidly with impact velocity and was as high as 2000 K for 5 km/s. However, this is only 10% of the binding energy

and not enough to rupture bonds during our simulations. PE normally becomes unstable at much lower temperatures and longer time scales when exposed to oxygen and other reactive molecules.

Initial equilibrations integrate the equations of motion using velocity Verlet with a 1 fs time step. They are performed in an *NPT* ensemble using a Nosé-Hoover thermostat and barostat with time constants of 0.25 and 2.0 ps, respectively. Dynamic shock simulations use a much lower 0.1 fs time step and are performed within an *NVE* ensemble, modeling adiabatic shock conditions. We monitored the energy throughout simulations to ensure that energy was conserved.

B. Initial configurations and equilibration

One amorphous and four crystalline samples were generated for dynamic impact simulations. All configurations have periodic boundary conditions in all three directions. The two box dimensions transverse to shock propagation are of approximately equal length, ranging between 5 and 17 nm. To test for finite-size effects, we performed several additional simulations for crystalline configurations with double the transverse box lengths. These simulations showed no observable difference in shock speed and mechanism of plastic deformation. The box dimension along the direction of shock must vary with the system in order to allow sufficient propagation time for accurate measurement of shock speeds. Shocks in amorphous PE and along the transverse [100] and [010] directions of the crystal require a propagation length of about 150 nm. Shock along the much stiffer crystal chain axis [001] required a substantially longer propagation length $\sim$300 nm, due to the fast-moving elastic precursor front (Sec. IV D). In order to measure the steady-state amplitude of the [001] elastic precursor, we had to generate an additional system about 1 μm long. In all cases, we align the shock axis with the z axis of the simulation box.

Amorphous configurations are prepared with the recently published method of Sliozberg *et al.* [37]. This melt equilibration method is a variant of the "fast push-off method" of Auhl *et al.* [38], and is fully described in Ref. [37]. $M = 1500$ chains of length $N = 1000$ are modeled by the united-atom potential of Paul *et al.* [39] and equilibrated at $T = 300$ K. After the united atom system is equilibrated, we reintroduce hydrogens along the chain backbones and perform a short energy minimization with AIREBO-M interactions to relax their positions. This is done with the FIRE minimizer and a time step of 15 fs. We then allow the system box to relax over 2 ns of *NPT* equilibration with a target $P = 1$ atm. This was sufficient time for the system density to equilibrate to a value of $\sim$825 kg/m^3.

Orthorhombic crystal configurations are made by copying the orthorhombic PE unit cell, which contains an ethylene from each of two chains, to make a supercell of the desired geometry. At 300 K and ambient pressure, AIREBO-M gives an orthorhombic unit cell with lattice vectors $(a, b, c) \approx$ (7.35, 4.94, 2.54) Å, which we align with the Cartesian axes of the simulation box. All chains are periodic, each connecting to itself across the periodic boundaries. This arrangement models chains with lengths much longer than our simulation

box dimensions, which would be typical for experimental molecular weights. Before shocking, we equilibrate crystals to $T = 300$ K and $P = 1$ atm for 100 ps in an *NPT* ensemble.

C. Shock generation

Following the approach in recent studies, we generate shocks by rigidly constraining a slab of molecules to impact the material as an effective rigid piston; see Fig. 2. After equilibration, the periodic boundary conditions along the shock direction are removed and atoms within 2.5 nm of the resulting boundaries are constrained to act as rigid slabs (dark gray in Fig. 2). For compressive shocks, the right slab is held fixed, while the left is constrained to move at a constant impact velocity $U_p = 100$–5000 m/s along the z axis [Fig. 2(a)]. The mobile slab acts as a rigid piston, compressing quiescent material (green) and imposing a jump in particle velocity to U_p (red material). This generates a shock front (red/green boundary) that propagates into the sample at a speed U_s. Data are collected until the shock front reaches the fixed rigid slab and is reflected.

While impacts initially compress material, coincident tensile deformation is often an important failure mechanism for oriented PE materials. To model tensile loading, the left slab is displaced leftward along z [Fig. 2(b)]. The systems were large enough for us to determine that neither amorphous nor crystalline PE produces steady shocks in tension (see Sec. IV).

Another common technique for generating shocks is to impact a finite sample with free boundaries upon a rigid wall that interacts with the material via power-law or idealized hard-wall interactions. He *et al.* recently showed that, except in regions very close to the piston, all these techniques generate essentially the same shock behavior [18]. A great advantage of the material piston technique we use is that it can generate shocks within systems prepared with periodic boundary conditions. There is no need to create and equilibrate free surfaces, which can be challenging for both crystalline and amorphous polymers. Free surfaces also introduce finite-size and edge effects which can complicate equilibration and measurement of bulk properties [40].

D. Analysis techniques

Shock waves drive systems into a nonequilibrium state, with sharp jumps in thermodynamic and hydrodynamic variables across the propagating front. In order to track this dynamic process, we must compute local measures of state variables. The system is divided into bins $\sim$1 nm wide along the shock direction. The average velocity u_i is obtained by a simple average over atoms in each bin. More care should be taken with the virial contributions to the local stress tensor, since they depend on multiple atoms that may be in different bins [41–43]. For the relatively coarse bins used here, partitioning the virial contributions evenly among the participating atoms was sufficient to capture the magnitude of discontinuities in the stress tensor at shock fronts. The element of the local stress
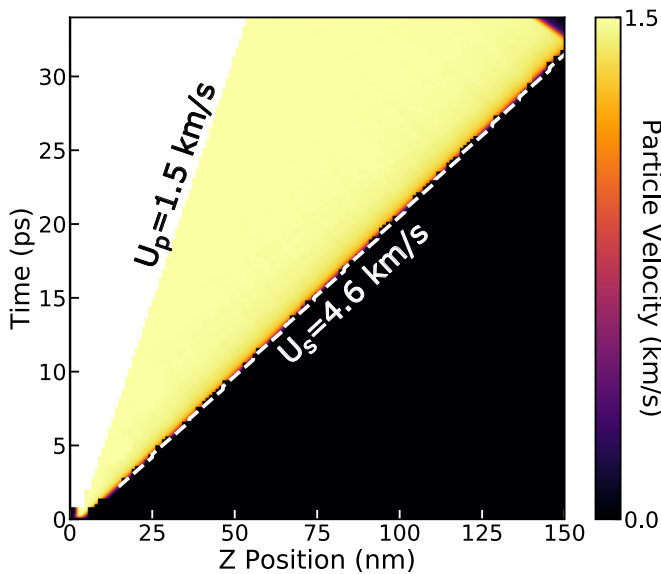
FIG. 3. Time evolution of particle velocity (u_z) profiles for the amorphous system in Fig. 2(a). The piston moves along z at $U_p = 1.5$ km/s, and is indicated by the white/yellow border. A shock traveling at U_s accelerates material from $u_z = 0$ (black) to $u_z = U_p$ (yellow). The white dashed line tracks the front where $u_z = 0.5U_p$. Least-squares fits to this line give $U_s \approx 4.6$ km/s.

tensor along Cartesian directions i and j was computed as

$$\sigma_{ij} = -\frac{1}{V_s} \sum_\alpha^{N\mathrm{bin}} \left[mu_i u_j + \frac{1}{2} \sum^{\mathrm{pairs}} (r_{i,1} f_{j,1} + r_{i,2} f_{j,2}) \right.$$
$$+ \frac{1}{3} \sum^{\mathrm{triples}} (r_{i,1} f_{j,1} + r_{i,2} f_{j,2} + r_{i,3} f_{j,3})$$
$$\left. + \frac{1}{4} \sum^{\mathrm{quads}} (r_{i,1} f_{j,1} + r_{i,2} f_{j,2} + r_{i,3} f_{j,3} + r_{i,4} f_{j,4}) \right]_\alpha, \quad (4)$$

where V_s is the volume of a bin, α indexes the atoms within a bin, u is an atom's velocity, and f_j is the force along j on atom α resulting from pairwise interactions or covalent bonds (pairs) or torsion interactions (triples and quads). The first term on the right of Eq. (4) represents the kinetic contribution to σ_{ij} and the remaining terms give the virial contributions to the stress.

The stresses of greatest interest are the shock stress $\sigma = \sigma_{zz}$ and characteristic shear stress $\tau = \sigma_{zz} - \frac{1}{2}(\sigma_{xx} + \sigma_{yy})$. The former is a measure of shock strength, while the latter is useful in determining the nature of any plasticity behind the shock front. For each system we present profiles of σ and τ along the shock direction in Sec. IV. Pastine's hydrostatic approximation requires that τ/σ_{zz} be small and deviations from his predictions for U_s in Fig. 1 are associated with large values of this ratio.

Stress and velocity profiles are calculated at 0.2 ps intervals for each shock simulation. Figure 3 visualizes one such time series for the particle velocities in the amorphous configuration of Fig. 2(a). The boundary of the white and yellow region is the piston traveling in the $+z$ direction at $U_p = 1.5$ km/s. The shock front accelerates material from $u_z = 0$ (black) to $u_z = U_p$ (yellow) and travels into the material at a speed $U_s > U_p$. To measure U_s we track the midpoint of the front, where $u_z = \frac{1}{2}U_p$

(white dashed line). U_s is obtained from a least-squares fit to the front position versus time. The standard error of a typical fit is less than 0.01 km/s. When the shock front reaches the far side of the sample, it reflects off the rigid material and back into the sample (small black triangle in upper right of Fig. 3). We do not analyze data after reflection occurs. The range of impact velocities studied, 0.1 to 5 km/s, overlaps with the experimental data shown in Fig. 1. We did not extend the simulations to higher U_p because shock produced conditions outside the range where AIREBO-M has been tested. As shown below, even for $U_p = 4$ km/s the pressure behind shock fronts is near 40 GPa. The corresponding temperature is about 1000 K. For $U_p = 5$ km/s the temperature nearly doubles and at higher velocities bond breaking and other effects may become important.

An advantage of studying shock with MD simulations is that they provide the explicit trajectories for all atoms as the shock transits the system. By analyzing these trajectories in tandem with dynamic profiles of σ and τ, we can identify specific plastic mechanisms that relax τ and "fluidize" the material. In Sec. IV we color atomic configurations either by particle velocity, the orientation of the zigzag carbon bonds along chain backbones, or by a local measure of deviatoric strain developed by Falk and Langer [42,44]. In the latter case, which we use to visualize [001] shocks, we use the relative motion within a radius of 15 Å to determine the strain. We choose this radius so that the strain measure captures the buckling of chain backbones which occurs at the scale of ∼100 Å.

IV. RESULTS AND DISCUSSION

A. Amorphous phase

Unaligned PE forms a semicrystalline structure at room temperature, with 40%–55% of the system in the amorphous phase [45]. Aligning PE by drawing reduces the amorphous content but does not eliminate it. About 5%–10% remains amorphous for highly drawn fibers [1]. Amorphous regions and their boundaries are typically much weaker than the crystal and can act as strength-limiting defects. Thus, characterizing the mechanical properties of purely amorphous PE is an essential step toward understanding the mechanics of the more complex and heterogeneous semicrystalline structures [7].

Compressive shocks with $U_p = 0.1$–3.5 km/s were generated in amorphous PE. A single plastic front formed for all cases—as illustrated in Fig. 2(a). Shock velocities obtained by tracking the shock front are plotted as purple pentagons in Fig. 1. For $U_p \geqslant 0.5$ km/s, U_s is a nearly linear function of U_p and agrees with Pastine's hydrostatic model. For lower impact velocities, the MD results lie above the hydrostatic predictions.

Stress profiles of the shocked configurations show that breakdown of hydrostatic behavior coincides with the weak-shock regime (large τ/σ). Figure 4 plots profiles of σ and τ at 13 ps after impact for several U_p from 0.3–3.5 km/s. Profiles are plotted as a function of distance from the moving piston ($z = 0$). Fronts propagate rightward, elevating σ and τ from 0 in the quiescent state at large z. When $U_p = 0.3$ km/s (blue), $\tau = 0.14$ GPa and $\sigma = 0.51$ GPa are similar in magnitude, explaining why U_s lies above the hydrostatic Hugoniot. As U_p increases, σ grows rapidly with increasing rate, while the rate
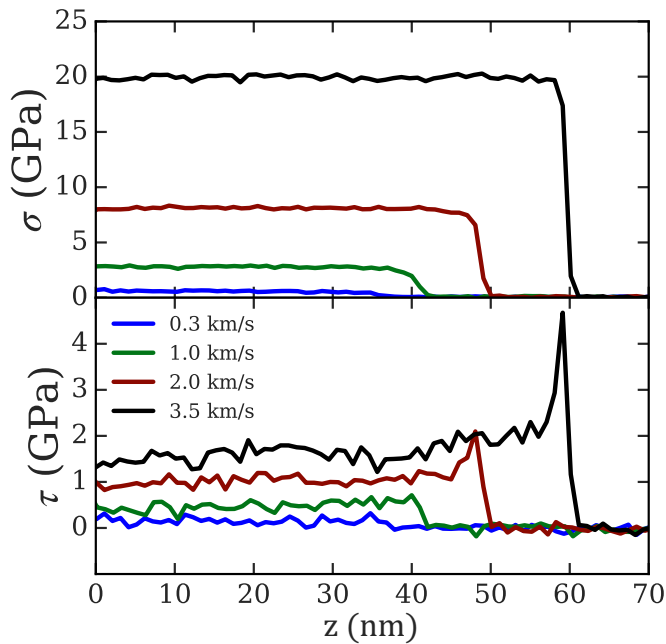
FIG. 4. Shock (σ) and shear (τ) stress profiles in amorphous PE for several U_p. All profiles are at $t = 13$ ps after impact and are plotted as a function of distance from the impacting piston. Shocks propagate to the right, elevating the stress from the quiescent state $\sigma = \tau = 0$. The rise in the steady value of σ with impact velocity becomes more rapid as U_p increases, while the rate of increase in τ is limited by plastic deformation. Hydrodynamic shock is recovered as τ/σ becomes small.

of increase of τ is limited by plastic deformation. This plastic relaxation leads to a rapid drop in τ/σ to ~0.075 at $U_p =$ 3.5 km/s (black), and recovery of hydrostatic shock behavior. Even for the lowest rates studied, plastic deformation is observed behind the shock front. A HEL may exist below $\sigma = 0.1$ GPa, but there may not be a sharp onset of plasticity since simulations have found that some plasticity always occurs when amorphous systems are strained [46].

We do not observe an elastic precursor wave for amorphous shock, indicating material is overdriven for even our lowest $U_p = 0.1$ km/s. This is reasonable given the low stiffness and strength of amorphous PE. Uniaxial compression simulations on the amorphous sample using an engineering strain rate of 10^8 s^{-1} give a Young's modulus $E \approx 1$ GPa and yield stress $\sigma_y \approx 50$ MPa. The former corresponds to a sound speed $c_s = (E/\rho)^{1/2} \approx 1.2$ km/s, which is about half of the slowest shock speed. Assuming $\sigma_{HEL} \sim \sigma_y$, we can estimate a maximum impact velocity $U_p \sim c_s\sigma_y/E \approx 60$ m/s before yield occurs. At this low U_p we face limitations similar to experiments; shocks are too weak for us to reliably track them above the thermal noise in our dynamic simulations.

We have also simulated amorphous PE in tensile shock loading. In this case, steady shock fronts do not form. Instead, strain localizes rapidly and nucleates a craze near the piston [Fig. 2(b)]. Once nucleated, further work by the piston goes towards growing the craze. Eventually the craze fractures, releasing the tensile load. The study of craze growth under high-rate loading and how it differs from quasistatic loading
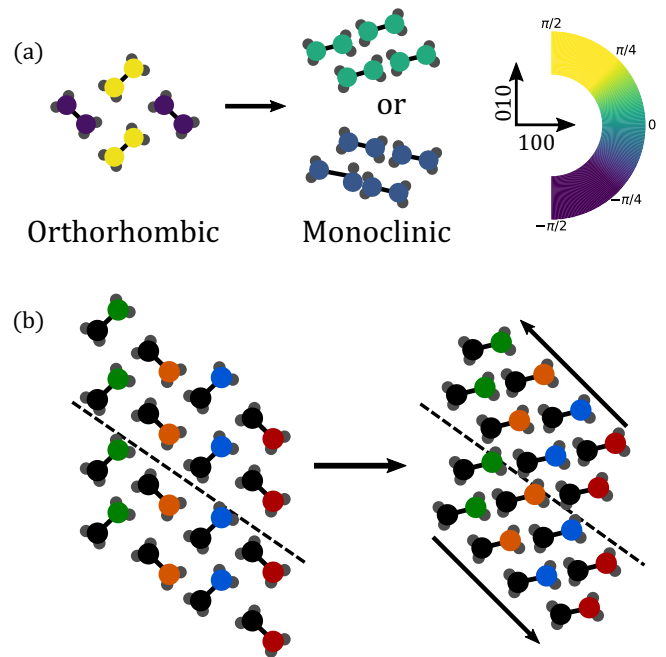

FIG. 5. Projections of atoms along chain backbones showing changes for impact along the horizontal [100] axis. (a) In the orthorhombic crystal (left), chains form a herringbone structure with alternating angles of ±43° to the [100] axis. Shock transforms regions into the monoclinic crystal structure (right) with all molecules aligned at an angle of ±20° to the [100] axis. Colors indicate orientation of the backbone relative to the [100] axis with the color map shown on the right. The same color map is used in Fig. 6. (b) A diagram showing how molecules rearrange into a monoclinic phase during [010] shock. One atom on each chain is colored to indicate successive (100) planes in order to show how molecules rotate and planes shear to form the monoclinic phase. All colored atoms are at the same height out of the page along [001] and the dashed line indicates a plane where shear occurs. Diagonal lines of molecules parallel to the dashed line rotate clockwise to move closer together. At the same time, chains reorient coherently to point in the same direction. The system shears by one chain spacing along the dotted line. This pattern repeats with shear along every second diagonal parallel to the dotted line.

is relevant to failure in many unaligned polymer materials. We defer analysis of this case to future work.

B. Shock along crystal *a* axis [100]

In the plane perpendicular to the chain backbone, chains pack in a "herringbone" structure with alternating orientations of the chain backbone to form an orthorhombic crystal [Fig. 5(a)]. This structure is determined by van der Waals interactions that have cohesive energies ~100 times weaker than backbone bonds [22]. The stiffness along the [100] direction is just 8 GPa compared to 260 GPa along the [001] direction. Because van der Waals interactions are both weak and nondirectional, chains can translate and rotate into new structures in response to applied loads, leading to complex crystal plasticity and crystal-crystal phase transitions. For example, experiments show pressure can convert some of a semicrystalline sample into a metastable monoclinic crystal [47,48]. Analytic and quantum chemistry studies have explored
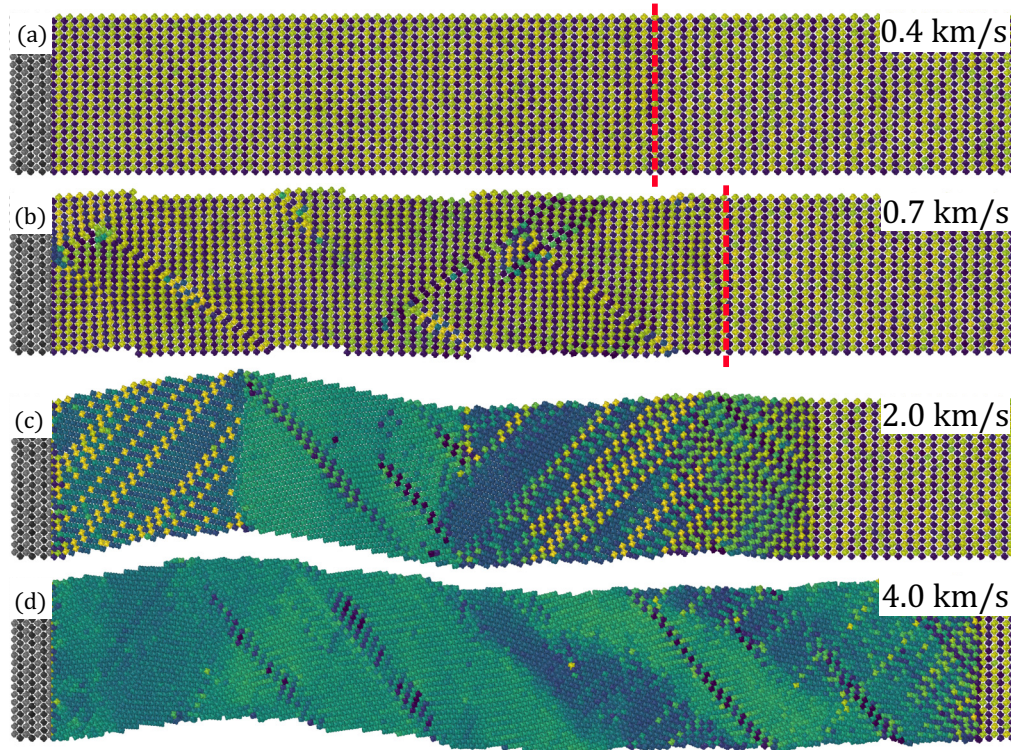
FIG. 6. Atomic configurations from a axis [100] shock simulations at $t = 14.4$ ps after impact for $U_p = 0.4, 0.7, 2.0$, and 4.0 km/s [(a)–(d)]. System dimensions are $9.84 \times 10.18 \times 157$ nm. The first ~ 63 nm along the z axis are shown in the rest frame of the piston (gray atoms) located at the far left. Chains are colored by the angle of the zigzag carbon backbone relative to the z axis [100]. As in Fig. 5, the herringbone structure of the orthorhombic crystal leads to alternating yellow and purple molecules. Monoclinic regions have uniform orientations corresponding to an aquamarine or medium blue (see color map in Fig. 5). (a) For $U_p = 0.4$ km/s there is a small increase in density behind the shock front (dashed line) but no plasticity. (b) For $U_p = 0.7$ km/s there is plastic deformation through slip along diagonal (110) planes. (c), (d) At higher velocities regions are deformed into monoclinic crystals with one of two orientations through the mechanism illustrated in Fig. 5(b).

thermodynamic stability of the monoclinic phase, but identifying specific transition mechanisms has remained an open question. As we now discuss, tracking atomic displacements allows us to identify how the monoclinic phase forms during shock when chains slip along the (110) plane and rotate collectively to locally reduce shear stresses.

Results for the shock velocity along the [100] direction are plotted as red circles in Fig. 1. The shock velocity shows a sharp break at $U_p = 0.7$ km/s. For $U_p \geqslant 0.7$ km/s, simulation results are in excellent agreement with Pastine's hydrostatic model. For $U_p < 0.7$ km/s, the shock velocity is systematically higher than hydrostatic predictions. We can identify the break in the U_p-U_s curve with the onset of crystal plasticity, i.e., the HEL. Shocks on the low-speed branch generate fully recoverable deformation. There is a small increase in density accompanied by small changes in backbone orientation as seen for 0.4 km/s in Fig. 6(a).

Shocks with $U_p \geqslant 0.7$ km/s cause plastic deformation. Figure 6(b) shows that at 0.7 km/s most chains are packed more tightly and retain the alternating orientations associated with the herringbone structure of the orthorhombic crystal. Plastic deformation occurs through shear by a nearest-neighbor chain spacing along some (110) planes of the orthorhombic crystal. This plane orientation has the largest resolved shear stress under uniaxial loading and shear along these planes leads to a local increase in density.

As U_p increases, shock produces a transition to the denser monoclinic phase. Figure 5(b) shows how molecules transform from orthorhombic to monoclinic order by shearing slightly along alternate diagonal (110) planes and rotating to have a uniform alignment. The two choices of shear plane lead to different orientations of the monoclinic structure with angle $\pm 12°$ to the z axis [Fig. 5(a)]. Figure 6(c) illustrates how this transition evolves for $U_p = 2.0$ km/s. Moving from the shock front to the left one sees a region where chains are beginning to lose the alternating herringbone orientation and adopt one of the two monoclinic orientations, corresponding to uniform regions of medium blue or aquamarine. There are twin boundaries between the two orientations. Figure 6(d) shows that increasing U_p to 4.0 km/s produces more complete conversion to the monoclinic state and an even greater increase in density.

Figure 7 shows profiles of σ and τ for the systems shown in Fig. 6. For $U_p = 0.4$ km/s, $\tau \sim \sigma \approx 1$ GPa. Between $U_p = 0.4$ km/s and $U_p = 4.0$ km/s, σ rises nonlinearly from about 1 GPa to 35 GPa. The value of τ remains near 1 GPa up to $U_p = 0.7$ km/s where plastic deformation first occurs. It then rises slowly with U_p and saturates near 3 GPa between 2–4 km/s. The strong saturation in τ implies a nearly hydrostatic pressure state behind the shock, and explains the agreement with the hydrostatic predictions at larger U_p.
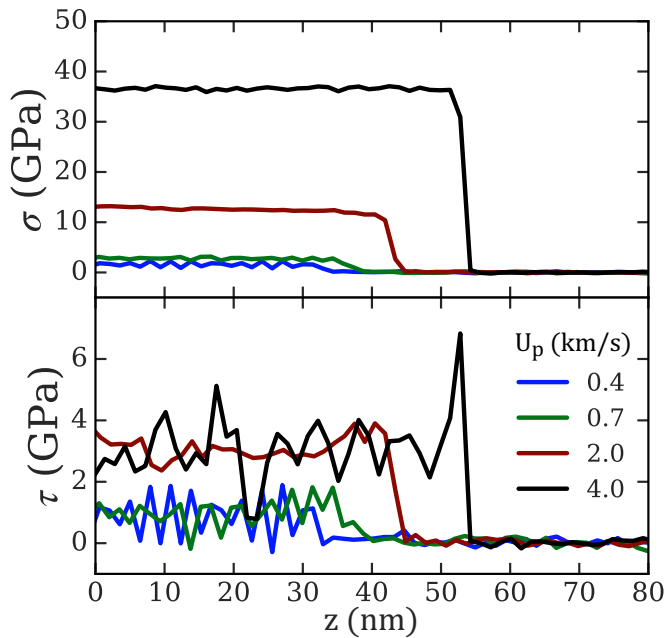
FIG. 7. Profiles of σ and τ as a function of distance from the piston z for the [100] shock configurations of Fig. 6, where $t = 14.4$ ps. (a) The shock stress rises rapidly with U_p. (b) The increase in shear stress is limited by plastic deformation and saturates for large U_p. The hydrostatic approximation becomes valid for $\sigma \gg \tau$.

From the above results, the HEL corresponds to a stress of $\sigma_{HEL} \sim 1$ GPa. Above this limit, we see no evidence of an elastic precursor, indicating shock above the HEL is always overdriven. We also do not observe separate plastic and phase transition fronts at high velocities, which we will show do occur for [010] shock. The region where plasticity develops remains narrow, rather than growing as the product of time and the difference between two front velocities.

C. Shock along crystal *b* axis [010]

Given the weak, nondirectional nature of van der Waals interactions, one might expect transverse shocks in PE to be relatively insensitive to the specific plane of impact. Indeed, many theories, textbooks, and experimental analyses approximate aligned PE crystals with transversely isotropic elasticity and plasticity, and thus predict direction-independent shock properties. While our simulations show the transverse Young's modulus is nearly isotropic, we find that the intimate coupling of chain translations and rotations during plastic flow leads to strong anisotropy in shock propagation.

Simulation results for U_s under impact along [010] are summarized by the green points in Fig. 1. One difference from the [100] results is that the jump indicating the onset of unrecoverable plastic deformation is much earlier, between 0.3 and 0.4 km/s instead of 0.6 and 0.7 km/s. A second difference is that the shock velocity for [010] rises above all other results between about 1.8 and 4.0 km/s. This implies a substantial rise in τ that is not relaxed by plastic deformation. In addition, for U_p between 2.8 and 4 km/s there is a second, slower shock front at which plasticity releases shear stress (open squares in Fig. 1).
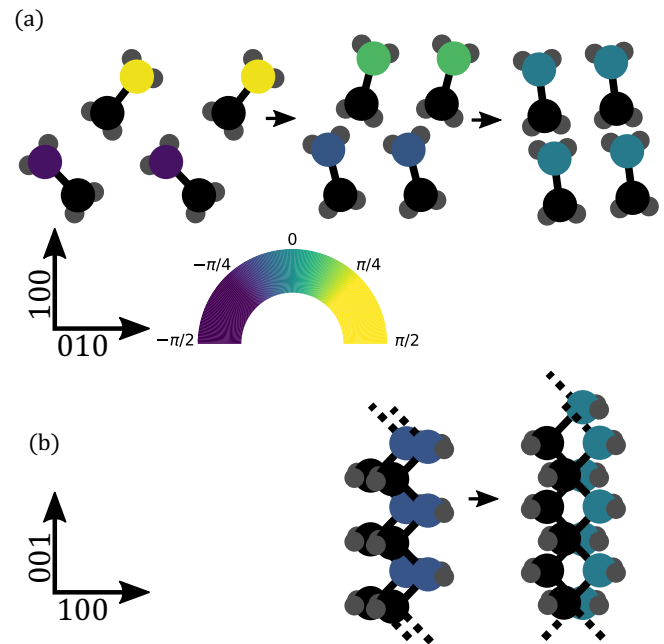

FIG. 8. Schematic showing crystals and transition paths for shock along [010]. (a) Projections along the chain axis. A pair of unit cells of the equilibrium orthorhombic crystal is shown on the left. Shock first compresses the crystal into a denser orthorhombic phase shown in the center. At very high pressures there is a further transition to a new structure. Colored atoms are at the same height into the page along [001] in the initial state and the color indicates the angle of the molecule relative to the [100] axis with the color map shown in the center. (b) Projections in the plane perpendicular to the [010] direction showing shear along alternate chains so that hydrogen atoms are at different heights to minimize steric repulsion.

We can understand the origin of the differences between [100] and [010] by contrasting the transverse deformation of the orthorhombic PE unit cell under strain. As illustrated in Fig. 5, the four chains in the initial unit cell are arranged in a herringbone pattern, forming a rhombus that is longer along [100] than [010]. When compressed along [100], the cell becomes more square. This arrangement is susceptible to slip along [110] with chain rotations producing the monoclinic transition discussed in the previous section and illustrated in Fig. 5. In contrast, compression along [010] makes the rhombus more asymmetric. As shown in Fig. 8, the unit cell collapses into a densely packed orthorhombic phase with chains rotating so their backbones are closer to the [100] direction. Although this phase has the same symmetry as the equilibrium structure, it appears to be a distinct phase separated by a free energy barrier due to steric constraints from the packing of hydrogens on different chains. A similar phase was observed in quasistatic MD simulations of crystalline PE at high pressures [22]. Chains in this phase are tightly interlocked and strong steric interactions hinder chain rotation and translation, suppressing (110) slip and monoclinic reorientations. The result is enhancement of the yield stress in the densely packed phase that produces deviations from the hydrostatic model.

For $U_p < 0.4$ km/s deformation is fully recoverable. For $0.4 \leqslant U_p \leqslant 1.6$ km/s, U_s is close to the hydrostatic model.
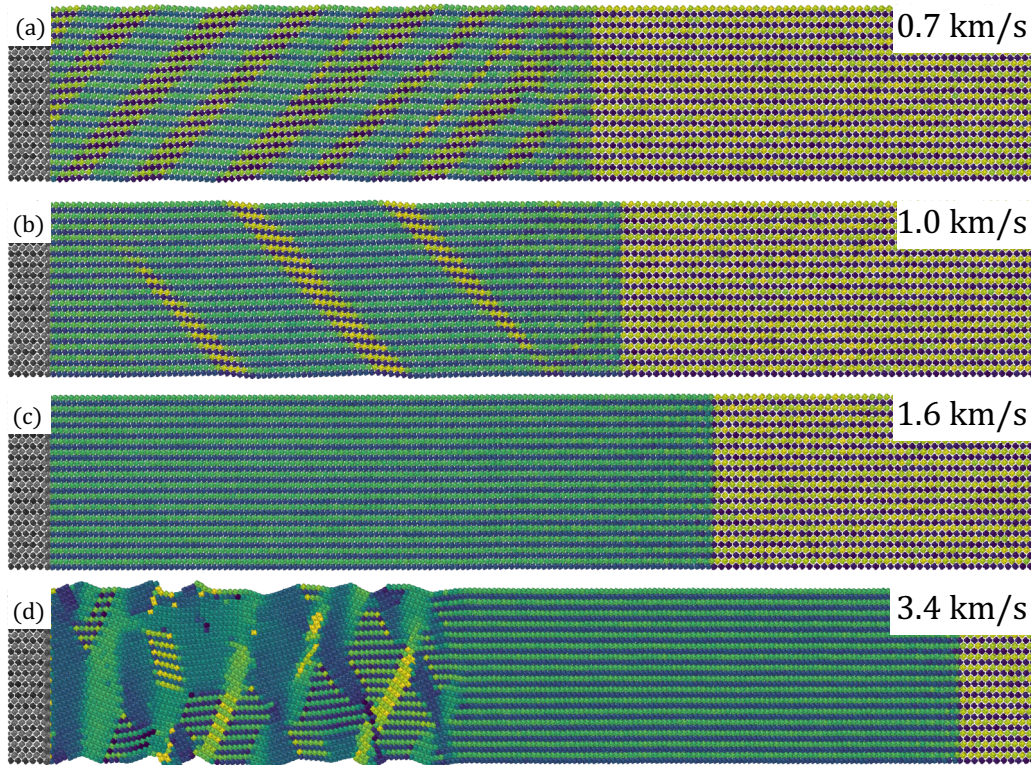
FIG. 9. Atomic configurations of b axis [010] shock simulations at $t = 10.0$ ps after impact for $U_p = 0.7, 1.0, 1.6$, and 3.4 km/s [(a)–(d)]. System dimensions are $10.2 \times 11.7 \times 153$ nm with only the first 70 nm along the z axis shown. Piston atoms are gray and other molecules are colored by their orientation relative to the vertical [100] axis. (a), (b) For $U_p < 1.6$ km/s, shock generates a banded structure with two coexisting orthorhombic crystal structures, the initial phase (yellow/purple) and a compressed phase (blue/green). Material slips at the boundary of these phases, relaxing shear. (c) At $U_p = 1.6$ km/s the entire system is converted into the compressed phase, which hinders chain slip and yield. (d) For U_p between 2.8 and 4.0 km/s there are two shock fronts. The first converts the system to the dense phase. At the second, the dense phase deforms plastically into domains of a new crystal structure. For $U_p \geqslant 4.0$ km/s the two fronts merge.

In this regime, the region behind the shock front contains coexisting regions of the two orthorhombic phases. As shown in Figs. 9(a)–9(c), the fraction of dense orthorhombic phase (alternating green/blue) grows with U_p and the entire region is in this phase for $U_p = 1.6$ km/s.

This transformation between phases should not be confused with the formation of multiple crystal grains through plastic deformation that is commonly observed in crystalline materials. Many materials exhibit coexisting crystal domains separated by grain boundaries. These grains are usually misoriented regions of the same crystal phase. The two distinct regions seen behind [010] shocks in Figs. 9(a)–9(c) are not reoriented domains of the same phase, but separate crystal structures. They both share orthorhombic symmetry, but have distinct lattice constants and unit-cell structure. In this system, the plastic process is the transformation of the initial unit cell into the second orthorhombic structure.

Figure 10 shows stress profiles for different U_p. When the two orthorhombic phases coexist, material shears easily along the diagonal phase boundaries, relaxing τ to ~ 1 GPa. The shear stress cannot easily relax when the entire region is in the dense phase. Strong steric interactions hinder chain rearrangement and suppress plasticity behind the front. This produces a substantial increase in τ with U_p, up to ~ 18 GPa for $U_p = 3.4$ km/s (Fig. 10), and elevates U_s above the hydrostatic shock speed.

Eventually shear stresses become large enough to initiate plasticity within the collapsed phase. This produces a two-front shock structure for U_p between 2.8 and 4.0 km/s. An example of the deformation behind each front is shown for $U_p = 3.4$ km/s in Fig. 9(d). At the first shock front, material is converted into the collapsed phase and τ rises dramatically to ~ 18 GPa (Fig. 10). This is followed by a plastic front where shear produces a transition to a new crystal structure and τ drops to ~ 4 GPa. The two-front structure is clear in the plot of τ in Fig. 10 but the plastic front produces very little change in σ.

The new phase behind the plastic front has a constant molecular orientation but is not the same as the monoclinic phase produced by [100] shocks. As shown in Fig. 8, chain reorientation is accompanied by translation of alternating chains by one carbon spacing along the chain backbone. This moves hydrogens on neighboring chains to different heights, allowing them to form an interdigitated structure that minimizes steric repulsion. As for the monoclinic phase in [100] shocks, there are two twins with molecular orientations corresponding to aquamarine and medium blue colors. Regions with these dense structures coexist with orthorhombic regions behind the plastic shock in Fig. 9(d).

Figure 11 shows the spatiotemporal variation in τ for three representative velocities. At $U_p = 2.6$ km/s there is a single jump in τ associated with the phase transformation
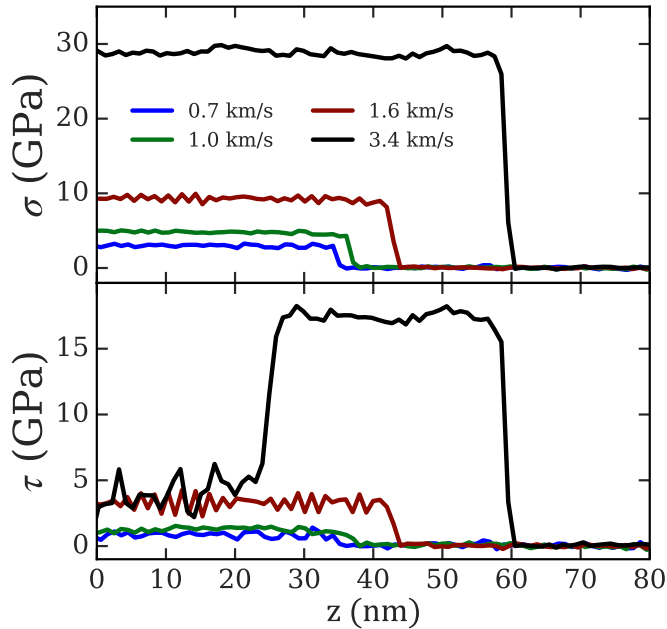
FIG. 10. Profiles of σ and τ as a function of distance from the piston for the [010] shock configurations of Figs. 9(a)–9(d) at $t =$ 10 ps after impact. The shock stress behind the front σ rises rapidly and nonlinearly with U_p. At velocities where the initial and dense orthorhombic phases coexist, material slips at phase boundaries and τ saturates at $\sim$2 GPa (blue and green curves). Once shocks fully compress chains into the dense phase, chain mobility is hindered and τ rises substantially. Sufficiently strong shocks nucleate plasticity in the compressed phase, producing a second plastic wave which unloads the shear stress (black curve).

to the dense orthorhombic phase [Fig. 11(a)]. For $U_p =$ 3.4 km/s there are two clear shock fronts propagating at different velocities [Fig. 11(b)]. As U_p increases, the velocity of the plastic front rises towards that of the phase transformation front. For $U_p \geqslant 4.0$ km/s the plastic front propagates at the same velocity. This is evident in Fig. 11(c), where the region

of dense orthorhombic crystal has a small constant width ahead of the plastically deformed state. In this high-velocity regime, the stress is nearly hydrostatic ($\tau/\sigma < 0.1$) and the [010] shock velocities coincide with the hydrostatic model.

D. Shock along crystal *c* axis [001]

1. Axial compression

The stiff backbone bonds aligned along the *c* axis of the PE crystal support a sound speed of $c_s \approx 16$ km/s that is greater than any U_s we measure. This leads to a two-wave "elastic-plastic" shock structure for compression along [001] [23]. As illustrated in the snapshots of σ for $U_p = 3.0$ km/s in Fig. 12, an elastic precursor propagates at the speed of sound (c_s) in the shock direction. This elevates the stress to the Hugoniot elastic limit (HEL). A plastic shock follows at a speed U_s (Fig. 1), relaxing the shear stress by activating plastic deformation mechanisms. We did not reach the overdriven limit for axial shock since the maximum $U_s \approx 11$ km/s for $U_p = 5.0$ km/s is well below $c_s = 16$ km/s. This is in sharp contrast to transverse and amorphous shock where no elastic precursor was observed and systems were overdriven.

As noted in Sec. II, the steady state amplitude of the elastic precursor stress should be independent of U_p and corresponds to σ_{HEL}, the shock analog of a quasistatic yield stress [23]. Shocks with amplitudes $\sigma > \sigma_{HEL}$ activate irreversible plastic mechanisms as they transit the system. For quasistatic compression, plasticity is known to occur through a chain buckling instability analogous to Euler buckling [28,49,50]. Understanding the dynamic buckling mechanism in shock is important for the design of fiber and fiber reinforced composite materials which often fail by buckling and kinking of fibers within the matrix material [51].

The curves in Fig. 12 show stress profiles of a $U_p = 3.0$ km/s shock at 7.5 ps intervals. Accurate resolution of the elastic precursor requires large propagation distances, so that the stress can be averaged over a large enough distance to remove thermal noise. This required about $\sim$50 ps and a system
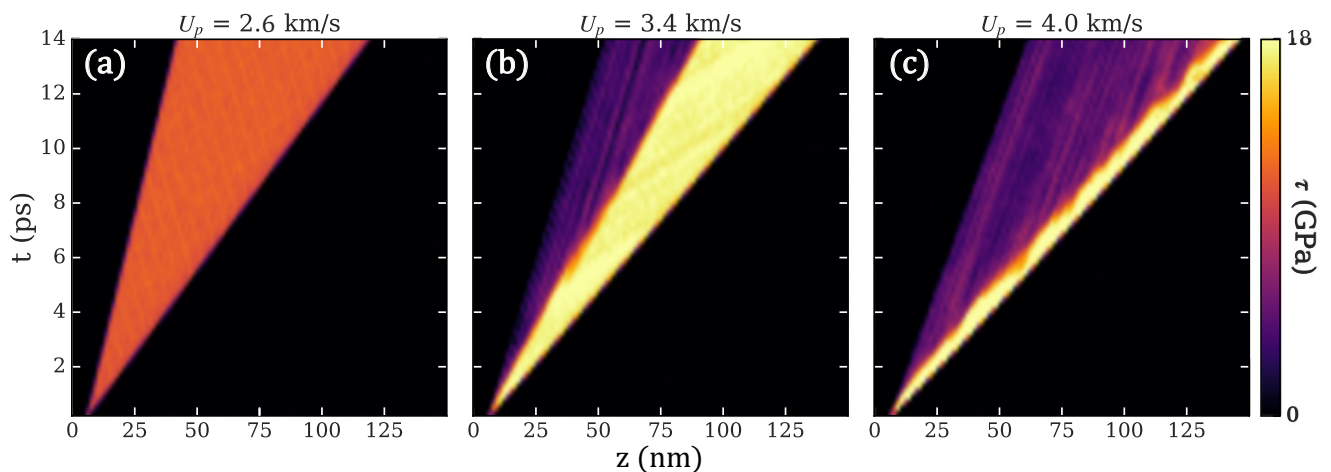

FIG. 11. Plots of the shear stress vs time and position for [010] shocks. (a) For $U_p = 2.6$ km/s there is a single shock that raises τ to 6.4 GPa. (b) For $U_p = 3.4$ km/s the first shock advances at $U_s = 9.5$ km/s and raises τ to 18 GPa. The second shock lowers τ to 4 GPa and moves at $U_s = 6.2$ km/s. (c) For $U_p = 4.0$ km/s the two shock fronts have merged into a region of fixed width that advances at $U_s = 10.0$ km/s.
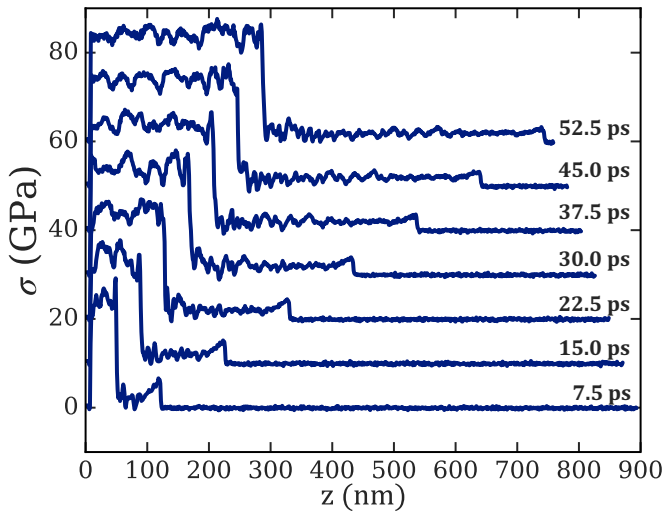
FIG. 12. Profiles of the shock stress (σ) at equal time intervals for a shock propagating 1 micron along [001] with $U_p = 3.0$ km/s. Successive profiles are offset vertically by 10 GPa to prevent overlap. The shock has a two-wave elastic-plastic structure, with the elastic precursor traveling at the adiabatic sound speed ~16 km/s. The precursor raises the stress to the HEL, $\sigma_{HEL} \approx 1.9$ GPa. Buckling occurs at the slower plastic front and raises σ above 20 GPa.

length of 1 μm, compared to 300 nm for determining U_s for plastic shocks. Taking the average stress at $t = 52.5$ ps for the full elastic region, we obtain an elastic limit $\sigma_{HEL} = 1.87$ GPa, corresponding to a piston velocity $U_p = 0.116$ km/s. This value is consistent with the critical buckling stress σ_c of PE under quasistatic loading. For a crystal with chains of length L and unit-cell area A

$$\sigma_c = \frac{\pi^2 EI}{AL^2} + G, \qquad (5)$$

where EI is the flexural rigidity and G is the shear modulus [28]. For long chains, $\sigma_c \approx G$. Calculating values of G along different crystallographic directions gives σ_c between 1.7 to 3.1 GPa, depending on the buckling direction. The lowest values are close to σ_{HEL} and correspond to buckling in the [010] plane.

Figure 13 shows molecular configurations at $t = 12$ ps after impact for U_p between 0.2 and 4.0 km/s. For $U_p <$ 0.116 km/s the system is below the HEL and there is no buckling or other plastic deformation. Above the elastic limit (Fig. 13), all systems show transverse fluctuations that develop into buckles. As expected from Eq. (5), buckles develop in the [010] plane where G is lowest. These buckles locally rotate the crystal structure, reducing the modulus along the propagation axis and facilitating the collapse of buckled material into a denser configuration behind the plastic shock front. The rotation angle tends to saturate at the value where successive chains can lock into registry by sliding by a lattice constant relative to their neighbors. This condition is met at $U_p = 1$ km/s. As U_p increases further, the frequency of the buckles increases.

The stress profiles for the above systems are shown in Fig. 14. The shock stress rises rapidly from about 2 GPa to almost 40 GPa while buckling allows the shear stress to relax

below 2 GPa a short distance behind the shock front. Note that this is comparable to the shear stress produced by the elastic shock that propagates ahead of the plastic shock. Although τ saturates for $U_p > 0.116$ km/s, Fig. 1 shows shock velocities lie below the hydrostatic predictions until $U_p \geqslant 2.0$ km/s. The hydrostatic prediction is based on conservation laws across a single interface. The elastic front carries part of the input energy ahead of the plastic shock front, reducing the drive at the plastic front and thus lowering its velocity. Since the pressure behind the elastic front is independent of U_p while the pressure behind the plastic front grows rapidly, U_s approaches the hydrostatic curve as U_p increases.

Extending our analysis to quantitatively predict how the two-wave structure influences U_s is not straightforward. While jump conditions for dual elastic-plastic wave forms can be derived, they usually assume that the material is both isotropic and linear elastic. Even then, the complexity of the constitutive equations usually requires numerical techniques to predict the structure and evolution of the shock waves [23]. Such approximations can work well for ductile metals, but are inappropriate for PE with its highly anisotropic and nonlinear elasticity. Continuum frameworks can be extended to anisotropic nonlinear elasticity and plasticity [52], but solutions require extensive numerical simulations that are beyond the scope of our study.

Analytic treatment of buckling kinematics is similarly challenging, but Fig. 13 illustrates several qualitative features worth noting. The plastic front shows a qualitative change in structure with increasing U_p. Plastic shocks with $U_p <$ 0.5 km/s form smooth bending undulations of the chain backbone, as in Fig. 13(a). Such bends are mediated by small deflections of dihedral angles around the trans conformation, and can be described by an elastic theory with an effective bending stiffness [28]. Buckles first form with a characteristic length scale of ~100 Å, which decreases with increasing U_p. We can understand this scale by revisiting the elastic arguments of Eq. (5). Previously, we considered buckling in the $L \rightarrow \infty$ limit where $\sigma_c \approx G$, and is independent of length. If instead we fix σ at some value above G and ask at what L buckling becomes favorable, we can extract a length scale. Consider the elastic precursor propagating in the axial direction at speed c_s. After a time δt, it has traveled a distance $L = c_s \delta t$, while the piston has compressed this material an amount $\delta L = U_p \delta t$, resulting in a stress $\sigma \approx E(\delta L/L) = E(U_p/c_s)$. Substituting this stress in Eq. (5) and solving for L^2 gives

$$L^2 = \frac{c_s}{U_p}\left(\pi^2 \frac{I}{A} + \frac{G}{E}\right) \approx \pi^2 \frac{c_s}{U_p}\frac{I}{A}, \qquad (6)$$

where the approximation on the right is valid for $G \ll E$. In this limit, $L \sim (U_p/c_s)^{-1/2}$, with a proportionality constant set by the geometry of the crystal unit cell. We can estimate the area moment I of the unit cell as that of a uniform rectangle, giving $I/A = \frac{1}{12}(a^2 + b^2) \approx 6.54$ Å^2. This gives $L \approx 94$ Å $= 37c$ for $U_p = 0.116$ km/s, consistent with our observations [Fig. 13(a)].

For $U_p \geqslant 0.5$ km/s, we observe a condensation of smoothly bending chains into sharp kinks, analogous to fold-crease transitions observed in thin sheets [Fig. 13(c)] [53–55]. Kinks form behind the shock front and are mediated by a series of consecutive gauche rotated dihedrals (green), which can be
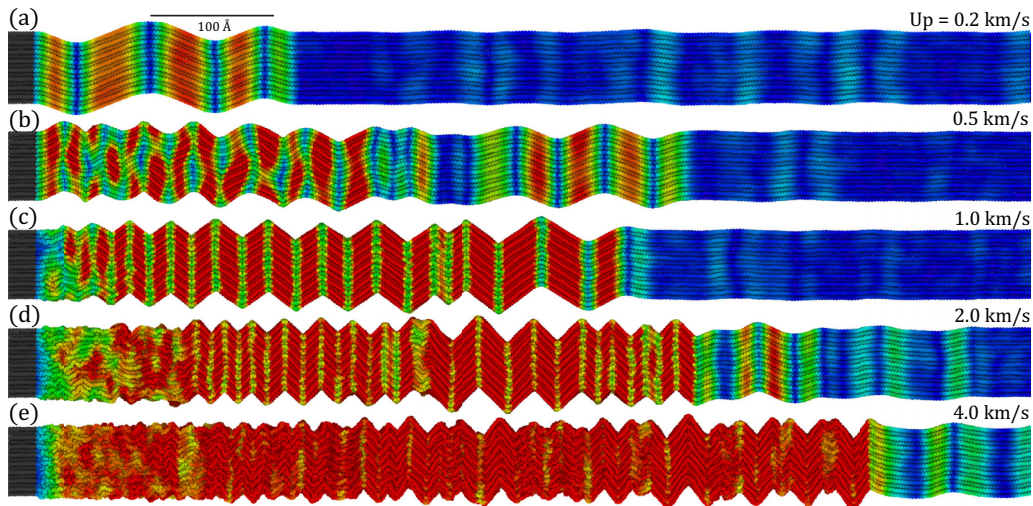
FIG. 13. Atomic configurations showing plasticity for c-axis [001] shock simulations at $t = 12$ ps after impact for $U_p = 0.2$–4.0 km/s [(a)–(e)]. System dimensions are $5.85 \times 5.41 \times 305$ nm. Plots are in the frame of reference of the left slab and only the leftmost 83 nm along the z axis are shown. The elastic shock has passed out of the field of view in all cases. Gray atoms belong to the piston and other atoms are colored according to the local strain (Sec. IIID) [42], with blue undeformed and green, orange, and red indicating progressively higher strain. Shock activates a buckling instability that sharpens into kinks mediated by a sequence of gauche dihedrals as U_p increases to 1.0 km/s. The characteristic length scale of buckles starts at $L \approx 100$ Å and decreases with increasing U_p.

considered a form of "bending plasticity." Buckles condense into kinks when the elastic bending energy overcomes the trans-gauche energy barrier. This transition can be associated with a critical curvature of chain bending that depends on the specific form of the dihedral energy. Increasing U_p drives kink

FIG. 14. Profiles of the shock stress (σ) and shear stress (τ) at $t = 12$ ps after impact for the [001] shock configurations in Fig. 13(a)–13(e). The value of σ rises rapidly with U_p. For $U_p > 0.116$ km/s ($\sigma > 1.87$ GPa) chains become unstable to buckling and collapse, keeping the value of τ behind the front below 2 GPa.

generation more rapidly, until kinks form almost immediately at the shock front [Figs. 13(d) and 13(e)].

2. Axial tension

Stable tensile (rarefaction) shocks are uncommon in most solids but can occur provided the material's stress-strain relationship possesses a region of positive curvature. A good example is Kolsky's generation of tensile shocks in vulcanized rubber, which are stabilized by the strain-hardening portion of the nonlinear stress-strain curve [56]. Unlike rubber, polyethylene crystals (and fibers) do not exhibit strain hardening [36,57,58]. Tensile shocks stretch the covalent backbone bonds of the chains. Covalent bond energies are anharmonic, showing decreasing stiffness as they dissociate. This produces a tensile stress-strain relation with negative curvature—i.e., large-amplitude tensile distortions travel slower than small-amplitude distortions [23,24]. Because of this property, crystalline PE does not form steady shock fronts in axial tension. Instead, tensile fronts disperse as they propagate—as illustrated in Fig. 15.

Figure 15 plots particle velocity profiles for $U_p = 1.4$ km/s tensile fronts at several consecutive times (solid lines). The profiles are shifted so that all are centered at the origin with the leading edge on the right. The front profile is not steady, but broadens linearly in time. This linear broadening implies that all profiles collapse onto a universal curve when the horizontal axis is divided by the corresponding time. Dashed lines show this collapse for $U_p = 1.4$ km/s and similar collapses were found for other $U_p \leqslant 1.6$ km/s. Bond anharmonicity also influences the overall speed of the tensile front, measured by tracking the midpoint of the jump in particle velocity. For low U_p, tensile fronts propagate at about the speed of sound $c_s = 16$
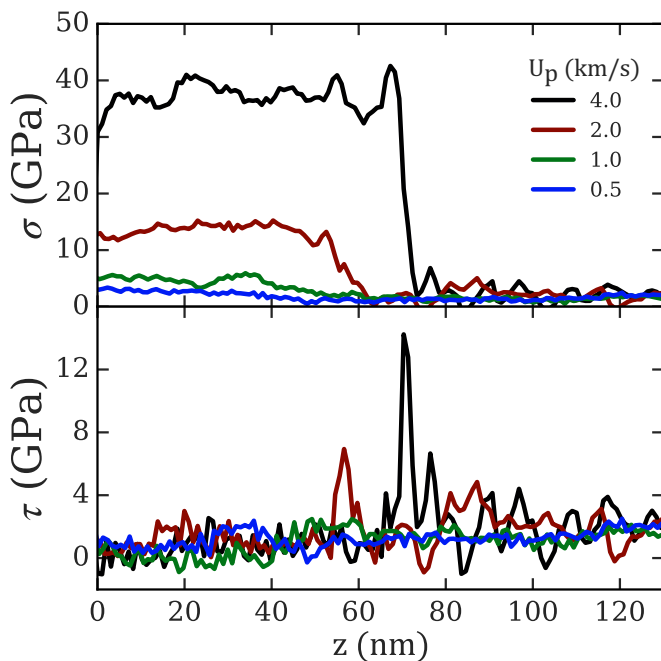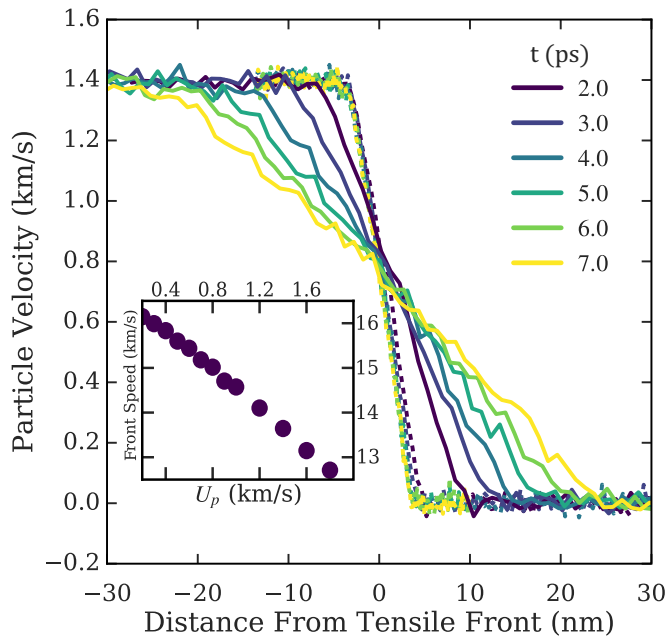
FIG. 15. Particle velocity profiles of a $U_p = 1.4$ km/s tensile front at uniform time intervals from $t = 2$ to 7 ps after tensile loading along [001] (solid lines). Fronts are shifted so the center is at the origin and the leading edge is to the right. Anharmonic softening of backbone bonds in tension causes the tensile front to broaden linearly in time. Dividing the horizontal axis by t collapses all profiles on a single curve (dashed lines). The group velocity of the front decreases with increasing U_p (inset).

FIG. 16. Atomic configurations for a $U_p = 2$ km/s tensile loading along [001] at $t = 2$, 4, and 6 ps. Two magnifications are shown for each time with a closeup (40 nm) above a larger view (136 nm). The piston (gray) moves leftward at 2 km/s and configurations are plotted relative to its position. Atoms are colored qualitatively by particle velocity, with red atoms moving leftward at U_p and blue atoms at rest. Chains fracture quickly after shock, forming a tensile pulse (green atoms) that propagates into the material at $\sim c_s$.

km/s. Increasing U_p leads to a linear drop in front speed, as shown in the inset of Fig. 15.

For simulations with $U_p \geqslant 1.8$ km/s, the crystal fails catastrophically by chain fracture. Figure 16 illustrates this behavior for $U_p = 2$ km/s. Atoms are colored by particle velocity for three consecutive times during the fracture process. Red atoms are traveling leftward with the piston at $u = U_p$, while blue atoms are at rest. Chain fracture unloads the tensile front, producing a finite-width tensile pulse that moves away from the piston (green atoms in Fig. 16). Other than their finite width, pulses show similar properties to the tensile fronts. They broaden over time and their group velocity decreases with increasing amplitude. The amplitude of pulses tends to decrease with increasing U_p, since fracture occurs more rapidly and unloads the crystal more effectively. At very large U_p, fracture is nearly instantaneous and generates very weak tensile pulses traveling with speed c_s.

We can compare the observed onset of chain fracture to quasistatic results. Uniaxial tension simulations with affine extension of the periodic box were done at $T = 300$ K and an engineering strain rate of 10^8 s^{-1} that is low enough for stress to equilibrate across the sample. Chains fractured at an engineering strain of about 0.11. For a tensile front traveling at the speed of sound, the effective engineering strain behind the front should be $\sim U_p/c_s$. This suggests we should observe fracture when $U_p \approx 0.11c_s \approx 1.76$ km/s, which agrees well with our dynamic measurements.

In this analysis we have studied an idealized PE crystal with effectively infinite chains (no chain ends). The only mode
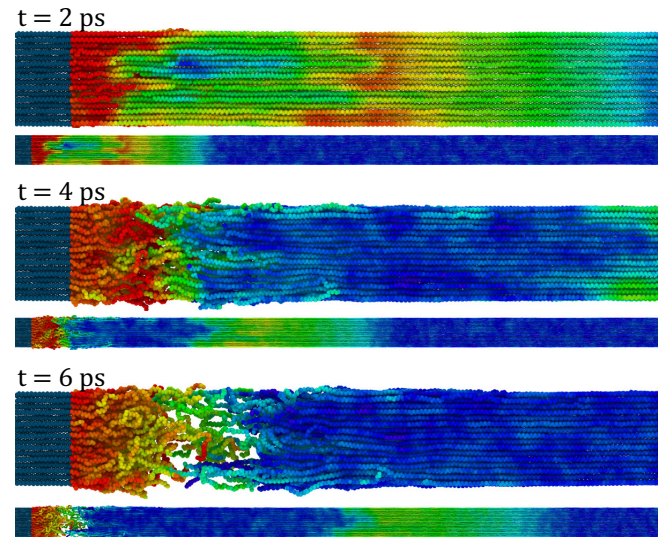
of tensile failure is fracture by chain scission. O'Connor and Robbins recently showed that PE crystals with chain ends do not yield by chain scission during quasistatic loading. Instead, chains slip by nucleating 1D dislocations at chain ends [36]. The presence of chain ends could modify the dynamic fracture process by introducing dislocations and slip as additional yield mechanisms. Whether chain slip would prevent scission during shock is not obvious. Both mechanisms could compete to relax shock-induced stresses, but if the rate of slip is slow relative to the rate of shock loading, then chain scission would still occur. We defer studying this competition of plastic relaxation mechanisms during high-rate loading to future work.

V. SUMMARY AND CONCLUSIONS

In this paper we studied shock loading of amorphous and crystalline polyethylene under both compressive and tensile loading with impact velocities from 100 m/s to 5 km/s. Tensile loading is common in applications of fibers in weaves and composites. Stable shock fronts are only expected when a material hardens under strain. Crystalline polyethylene does not strain harden under tension and no stable shock front was observed. Amorphous samples fail through craze formation, growth, and fracture near the loading region. Crystals in fibers are typically aligned with chain backbones along the fiber. Tensile loading in this direction at $U_p < 2$ km/s produces a front that broadens linearly with time rather than a true shock front. The tension behind the front grows with U_p, and for $U_p \geqslant 2$ km/s the system fails through chain fracture. We expect that this may be an upper bound for fracture in semicrystalline fibers since amorphous regions, chain ends,

and other defects not included in our simulations will facilitate fracture.

Compressive loading of amorphous PE produces simple shock fronts. Because the yield stress is low, the shock velocity agrees with Pastine's hydrostatic model for $U_p \geqslant 0.5$ km/s. For $U_p = 0.3$ km/s the shear stress behind the shock front is about a quarter of the compressive stress and U_s is about 10% above Pastine's prediction. The discrepancy grows with decreasing U_p. No elastic precursor was observed and we estimate that the system will remain overdriven until U_p is lower than about 60 m/s.

Compressive loading of crystals produces strongly anisotropic behavior with a wide range of shock structures related to different modes of plastic deformation and crystal phase transformations. This variety of behavior can only be captured by a fully atomistic treatment of interactions. Hugoniot elastic limits were identified for shock along the three principal crystal directions and associated with direction-specific plastic deformation mechanisms.

Elastic precursor fronts were only observed for loading along the chain axis where the sound velocity (16 km/s) is much higher than in other directions (∼3 km/s) and also larger than the highest impact velocities studied (5 km/s). The stress behind the elastic precursor gave $\sigma_{HEL} = 1.87$ GPa, corresponding to $U_p = 0.116$ km/s at the elastic limit. As expected from this result, simulations at $U_p = 0.1$ km/s showed no plastic deformation. At $U_p \geqslant 0.2$ km/s, loading along the chain backbone produced transverse fluctuations that developed into buckles in the [010] plane where the shear stress $G = 1.7$ GPa is lowest. The buckles increase the density by compressing the weaker intermolecular bonds instead of the strong covalent backbone bonds. In the long-wavelength limit the critical buckling stress approaches G and the observed σ_{HEL} is close to the value of G in the [010] plane. Including the wavelength dependence [Eq. (5)] we find that the driving stress at $U_p = 0.2$ km/s should produce a wavelength of 94 Å, which is close to the observed wavelength in Fig. 13(a). The wavelength of buckles decreases as U_p increases and the buckles sharpen into kinks for $U_p \geqslant 1$ km/s. Between kinks, chains rotate to an angle where neighboring chains have slipped laterally by about a lattice constant so that hydrogens on neighboring chains pack efficiently at high density. As U_p increases, this angle remains nearly constant but the spacing between kinks decreases. By $U_p = 4$ km/s the kink spacing is only a few monomers and the structure becomes more disordered.

The linear response in the plane perpendicular to chain backbones is nearly isotropic, but shock leads to highly anisotropic deformation mechanisms. Shock along the [100] axis produces a single shock front. At impact velocities $U_p < 0.7$ km/s, shock produces recoverable deformation and U_s lies above Pastine's hydrostatic prediction. Plasticity occurs above the HEL, corresponding to $U_p \approx 0.7$ km/s. Initially plasticity involves slip along (110) planes. As U_p increases, more and more of the material is converted into a monoclinic phase with two twin orientations. Shear along twin boundaries helps to relieve shear stress, leading to fairly hydrostatic conditions. Experiments have also found evidence for formation of a monoclinic phase under compression [48,59].

For shock along the [010] direction, plasticity sets in at a lower velocity of $U_p \sim 0.5$ km/s. For $U_p < 1.6$ km/s,

plasticity produces a banded structure where a dense orthorhombic phase coexists with the equilibrium orthorhombic phase. For $U_p \geqslant 1.6$ km/s the entire system converts to the dense phase, which has a very high yield stress. For U_p between 2.8 and 4.0 km/s there is a two-front structure. The first is a transformation front, that produces the dense orthorhombic phase and has a shock velocity above Pastine's theory because of the large yield stress. The second is a plastic front where the deformation relaxes the shear stress. The dense orthorhombic phase is deformed into a new monoclinic structure through chain rotation and translation of alternating chains along the chain backbone. Shear along the boundary between two twins of the monoclinic structure relieves the shear stress. For $U_p > 4.0$ km/s one can still identify a region of dense orthorhombic phase ahead of the monoclinic structures. However, this dense region has a constant width and is thus part of a single shock front with a velocity near Pastine's prediction.

Real crystalline PE contains crystal defects such as chain ends and amorphous inclusions, which can substantially alter the crystal's mechanics and plasticity [30,36]. Additionally, amorphous phases in processed PE can be substantially aligned and denser than in unprocessed samples. In a companion paper, Elder *et al.* applied similar MD techniques to show crystal-amorphous phase boundaries in oriented PE reflect shocks and significantly attenuate shock energy [30]. It was also shown that shock propagation through amorphous PE is sensitive to density and alignment. Continued study is needed to understand how additives, defects, and nanoscale heterogeneity scatter shocks and compete with the plastic mechanisms we identify here.

PE is never purely amorphous or crystalline in applications. Further studies are needed to better understand how phase heterogeneity modifies shock behavior. While a mean-field mixing of pure-phase Hugoniots is sufficient to capture shocks in isotropic semicrystalline PE [6], this approach is unlikely to succeed for processed PE in fibers and composites. These anisotropic systems exhibit complex hierarchies of crystal and amorphous phases which span from nanometer to millimeter scales [60]. Capturing such structures is beyond the scope of molecular simulations, but our pure phase data should be valuable input for micromechanics models which can capture PE's mesoscale structure. Continued multiscale investigation could identify strategies for tuning shock absorption in high-performance PE.

[1] B. Crist, Annu. Rev. Mater. Sci. **25**, 295 (1995).

[2] A. Kelly and N. H. Macmillan, *Strong Solids* (Oxford University Press, Oxford, UK, 1986).

[3] K. Tashiro, M. Kobayashi, and H. Tadokoro, Macromolecules **11**, 914 (1978).

[4] H. van der Werff and A. J. Pennings, Colloid Polym. Sci. **269**, 747 (1991).

[5] R. Marissen, Mater. Sci. Appl. **2**, 319 (2011).

[6] W. Carter and S. Marsh, Hugoniot equation of state of polymers, Tech. Rep. LA-13006-MS, Los Alamos National Laboratory, 1995.

[7] D. J. Pastine, J. Chem. Phys. **49**, 3012 (1968).

[8] D. J. Pastine, in *Propriétés Physiques des Solides Sous Pression* (CNRS, Paris, 1970).

[9] J. Colvin and J. Larsen, *Extreme Physics: Properties and Behavior of Matter at Extreme Conditions* (Cambridge University Press, Cambridge, 2013).

[10] B. L. Holian, Phys. Rev. A **37**, 2562 (1988).

[11] B. L. Holian and P. S. Lomdahl, Science **280**, 2085 (1998).

[12] T. C. Germann, B. L. Holian, P. S. Lomdahl, and R. Ravelo, Phys. Rev. Lett. **84**, 5351 (2000).

[13] M. Grujicic, B. Pandurangan, W. C. Bell, B. A. Cheeseman, C. F. Yen, and C. L. Randow, Mater. Sci. Eng. **528**, 3799 (2011).

[14] B. Arman, Q. An, S. N. Luo, T. G. Desai, D. L. Tonks, T. Çağın, and W. A. Goddard, J. Appl. Phys. **109**, 013503 (2011).

[15] T. L. Chantawansri, T. W. Sirk, E. F. C. Byrd, J. W. Andzelm, and B. M. Rice, J. Chem. Phys. **137**, 204901 (2012).

[16] S. Root, T. A. Haill, J. M. D. Lane, A. P. Thompson, G. S. Grest, D. G. Schroen, and T. R. Mattsson, J. Appl. Phys. **114**, 103502 (2013).

[17] J. M. D. Lane, G. S. Grest, and T. R. Mattsson, Comput. Mater. Sci. **79**, 873 (2013).

[18] L. He, T. D. Sewell, and D. L. Thompson, J. Appl. Phys. **114**, 163517 (2013).

[19] M. G. Fröhlich, T. D. Sewell, and D. L. Thompson, J. Chem. Phys. **140**, 024902 (2014).

[20] Y. Fu, J. Michopoulos, and J.-H. Song, J. Polym. Sci., Part B: Polym. Phys. **53**, 1292 (2015).

[21] F. Xie, Z. Lu, Z. Yang, W. Hu, and Z. Yuan, Polymer **98**, 294 (2016).

[22] T. C. O'Connor, J. Andzelm, and M. O. Robbins, J. Chem. Phys. **142**, 024903 (2015).

[23] L. Davison, *Fundamentals of Shock Wave Propagation in Solids* (Springer-Verlag, Berlin, Heidelberg, 2008).

[24] J. Forbes, *Shock Wave Compression of Condensed Matter: A Primer* (Springer, Berlin, 2013).

[25] R. Ravelo, T. C. Germann, O. Guerrero, Q. An, and B. L. Holian, Phys. Rev. B **88**, 134101 (2013).

[26] J. N. Johnson, J. Appl. Phys. **42**, 5522 (1971).

[27] D. Bancroft, E. L. Peterson, and S. Minshall, J. Appl. Phys. **27**, 291 (1956).

[28] S. J. DeTeresa, R. S. Porter, and R. J. Farris, J. Mater. Sci. **20**, 1645 (1985).

[29] D. Hossain, M. A. Tschopp, D. K. Ward, J. L. Bouvard, P. Wang, and M. F. Horstemeyer, Polymer **51**, 6071 (2010).

[30] R. M. Elder, T. C. O'Connor, T. L. Chantawansri, Y. R. Sliozberg, T. W. Sirk, I.-C. Yeh, M. O. Robbins, and J. W. Andzelm, Phys. Rev. Mater. **1**, 043606 (2017).

[31] T. R. Mattsson, J. M. D. Lane, K. R. Cochrane, M. P. Desjarlais, A. P. Thompson, F. Pierce, and G. S. Grest, Phys. Rev. B **81**, 054103 (2010).

[32] M. Lísal, J. K. Brennan, and J. B. Avalos, J. Chem. Phys. **135**, 204105 (2011).

[33] S. Plimpton, J. Comput. Phys. **117**, 1 (1995).

[34] D. W. Brenner, O. A. Shenderova, J. A. Harrison, S. J. Stuart, B. Ni, and S. B. Sinnott, J. Phys.: Condens. Matter **14**, 783 (2002).

[35] L. Pastewka, P. Pou, R. Pérez, P. Gumbsch, and M. Moseler, Phys. Rev. B **78**, 161402 (2008).

[36] T. C. O'Connor and M. O. Robbins, ACS Macro Lett. **5**, 263 (2016).

[37] Y. R. Sliozberg, M. Kröger, and T. L. Chantawansri, J. Chem. Phys. **144**, 154901 (2016).

[38] R. Auhl, R. Everaers, G. S. Grest, K. Kremer, and S. J. Plimpton, J. Chem. Phys. **119**, 12718 (2003).

[39] W. Paul, D. Y. Yoon, and G. D. Smith, J. Chem. Phys. **103**, 1702 (1995).

[40] K. Kadau, T. C. Germann, P. S. Lomdahl, and B. L. Holian, Phys. Rev. B **72**, 064120 (2005).

[41] B. D. Todd, D. J. Evans, and P. J. Daivis, Phys. Rev. E **52**, 1627 (1995).

[42] M. L. Falk and J. S. Langer, Phys. Rev. E **57**, 7192 (1998).

[43] F. Varnik, J. Baschnagel, and K. Binder, J. Chem. Phys. **113**, 4444 (2000).

[44] F. Shimizu, S. Ogata, and J. Li, Mater. Trans. **48**, 2923 (2007).

[45] I. M. Ward and J. Sweeney, *Mechanical Properties of Solid Polymers* (John Wiley & Sons, 2012).

[46] J. Rottler and M. O. Robbins, Phys. Rev. E **64**, 051801 (2001).

[47] L. Lin and A. S. Argon, J. Mater. Sci. **29**, 294 (1994).

[48] K. Russell, B. Hunter, and R. Heyding, Polymer **38**, 1409 (1997).

[49] M. R. McGann and D. J. Lacks, Macromolecules **31**, 6356 (1998).

[50] M. R. McGann and D. J. Lacks, Phys. Rev. Lett. **82**, 952 (1999).

[51] J. Lankford, J. Mater. Sci. **30**, 4343 (1995).

[52] J. M. Winey and Y. M. Gupta, J. Appl. Phys. **96**, 1993 (2004).

[53] D. P. Holmes and A. J. Crosby, Phys. Rev. Lett. **105**, 038303 (2010).

[54] H. King, R. D. Schroll, B. Davidovitch, and N. Menon, Proc. Natl. Acad. Sci. USA **109**, 9716 (2012).

[55] F. Brau, P. Damman, H. Diamant, and T. A. Witten, Soft Matter **9**, 8177 (2013).

[56] H. Kolsky, Nature (London) **224**, 1301 (1969).

[57] M. Hudspeth, X. Nie, and W. Chen, Polymer **53**, 5568 (2012).

[58] M. Hudspeth, B. Claus, N. Parab, B. Lim, W. Chen, T. Sun, and K. Fezza, Journal of Dynamic Behavior of Materials **1**, 55 (2015).

[59] L. Fontana, M. Santoro, R. Bini, D. Q. Vinh, and S. Scandolo, J. Chem. Phys. **133**, 204502 (2010).

[60] P. B. McDaniel, J. M. Deitzel, and J. W. Gillespie, Polymer **69**, 148 (2015).